

Tuning scalar spin chirality in ultrathin films of the kagome-lattice ferromagnet Fe₃Sn

Kohei Fujiwara¹✉, Yasuyuki Kato², Takeshi Seki^{1,3}, Kentaro Nomura^{1,3}, Koki Takanashi^{1,3,4}, Yukitoshi Motome² & Atsushi Tsukazaki^{1,3,4}

Non-coplanar spin textures with finite scalar spin chirality can be artificially induced at surfaces and interfaces through the interfacial Dzyaloshinskii-Moriya interaction. However, stabilizing a proper magnetic skyrmion crystal via this route remains elusive. Here, using an epitaxial bilayer of platinum and geometrically frustrated kagome-lattice ferromagnet Fe₃Sn, we show the possible formation of a two-dimensional skyrmion crystal under well-regulated Fe₃Sn thickness conditions. Magnetization measurements reveal that the magnetic anisotropy is systematically varied from an inherent in-plane type to a perpendicular type with the thickness reduction. Below approximately 0.5 nm, we clearly detect a topological Hall effect that provides evidence for finite scalar spin chirality. Our topological Hall effect analysis, combined with theoretical simulations, not only establishes its interfacial Dzyaloshinskii-Moriya interaction origin, but also indicates the emergence of a stable skyrmion crystal phase, demonstrating the potential of kagome-lattice ferromagnets in spin chirality engineering using thin-film nanostructures.

¹Institute for Materials Research, Tohoku University, Sendai 980-8577, Japan. ²Department of Applied Physics, University of Tokyo, Tokyo 113-8656, Japan. ³Center for Spintronics Research Network (CSRN), Tohoku University, Sendai 980-8577, Japan. ⁴Center for Science and Innovation in Spintronics (CSIS), Core Research Cluster, Tohoku University, Sendai 980-8577, Japan. ✉email: kohei.fujiwara@tohoku.ac.jp

Scalar spin chirality, $\mathbf{S}_i \cdot (\mathbf{S}_j \times \mathbf{S}_k)$, is a quantity that corresponds to a solid angle subtended by three spins \mathbf{S}_i , \mathbf{S}_j , and \mathbf{S}_k on neighboring triangular sites^{1–3}. Electrons hopping through non-coplanar spin textures with finite scalar spin chirality acquire Berry phase equivalent to a fictitious magnetic field, leading to topological Hall effect (THE)^{4,5} that is distinct from other Hall effects. Among various non-coplanar spin textures, a swirling spin texture called the magnetic skyrmion^{4–6} is particularly interesting because it can not only behave like an individual particle-like object but also can form an ordered skyrmion crystal (SkX) under the delicate competition of magnetic interactions and external perturbations. Understanding the stability and controllability of SkX phase is currently at the frontier of condensed matter research.

The established approach for the formation of SkX phase is to use noncentrosymmetric bulk crystals^{4,5} in which finite contributions of spin-orbit coupling (SOC) induce the Dzyaloshinskii-Moriya interaction (DMI)^{7,8}, expressed as $H_{\text{DMI}} = -\mathbf{D} \cdot (\mathbf{S}_i \times \mathbf{S}_j)$ with \mathbf{D} being the DMI vector. This interaction favors a relative twist between otherwise parallel or anti-parallel spins, giving rise to complex magnetic states such as canted ferromagnetism^{7,8}, non-coplanar and helical/spiral spin states^{4,5}. In thin-film heterostructures, the role of SOC in bulk crystals can be activated by fabricating an asymmetric interface with individual magnetic and SOC layers, which is known as the interfacial DMI^{9,10}. In various interface systems including metals^{11–16}, perovskite-type oxides^{17,18}, and topological insulators^{18,19}, the formation of isolated skyrmions and the detection of THE have been reported. However, the two-dimensional SkX has rarely been achieved by the interfacial DMI mechanism²⁰. Given the crucial role of crystal symmetry in the bulk approaches, a choice of specific lattice systems that enable the tuning of complex magnetic interactions is essential.

With this perspective, we focused on kagome-lattice magnets with a triangular-based lattice, which is suitable for inducing non-coplanar magnetic states required for the SkX phase. We selected a ferromagnetic intermetallic compound Fe_3Sn with the $D0_{19}$ structure. Bulk Fe_3Sn is ferromagnetic below Curie temperature T_c of 743 K with in-plane magnetic anisotropy in the Fe_3Sn kagome plane (ab plane)²¹. Very recently, it has been reported that Fe_3Sn can be epitaxially grown as a thin film on Pt(111) (ref. 22). The combination of Fe_3Sn and Pt offers the following advantages for spin chirality engineering via the interfacial DMI: (i) Fe_3Sn consists of ideal two-dimensional kagome planes (Fig. 1a), (ii) the epitaxial interface across Pt with strong SOC effectively activates the interfacial DMI, (iii) large magnetization derived from Fe enables the characterization of magnetic properties in the ultrathin films.

Here, we report a comprehensive study that strongly suggests the formation of a two-dimensional SkX phase in $\text{Fe}_3\text{Sn}/\text{Pt}$ epitaxial bilayers (Fig. 1a). By tuning the magnetic anisotropy and the interfacial DMI via the reduction of the Fe_3Sn thickness, t , we attempt to achieve the non-coplanar spin state with finite scalar spin chirality (Fig. 1b, c). The evolution of magnetic anisotropy and the occurrence of THE revealed by the systematic t -dependent measurements are consistent with the formation of SkX in a theoretical model based on a ferromagnetic kagome lattice.

Results and discussion

Fabrication of kagome-lattice $\text{Fe}_3\text{Sn}/\text{Pt}$ bilayers. We fabricated t -nm-thick $\text{Fe}_3\text{Sn}/10$ -nm-thick Pt bilayers on $\text{Al}_2\text{O}_3(0001)$ substrates by radio-frequency magnetron sputtering (see Methods). Figure 1d displays a cross-sectional transmission electron microscopy (TEM) image of a bilayer sample with $t = 8$ nm. The selected-area electron diffraction, shown in Fig. 1e, together with the macroscopic X-ray diffraction (Supplementary Fig. 1), identifies the crystallization of the high-temperature Fe_3Sn phase

(JCPDS PDF 01-074-5857) with an epitaxial orientation relationship of $\text{Fe}_3\text{Sn}[01\bar{1}0](0001)/\text{Pt}[11\bar{2}](111)/\text{Al}_2\text{O}_3[11\bar{2}0](0001)$ (see Supplementary Fig. 2 for the analysis of fast Fourier transformation diffraction patterns). The well-crystallized and homogeneous growth of Fe_3Sn was also observed for $t = 1.6$ nm (Supplementary Fig. 3). Because it is difficult to apply the same analysis to much thinner films ($t < 1$ nm) shown below, we hereafter adopt the nominal t value based on the sputtering rate assuming uniform film deposition. As shown in Fig. 1f, M versus magnetic field $\mu_0 H$ curves (where μ_0 is vacuum permeability and H is magnetic field strength) measured for $t = 0.80$ nm (~ 2 unit cells, the bulk c -axis length = 0.436 nm) in an out-of-plane H show hard-axis behavior without remanent M (see Supplementary Fig. 4 for the data of other t values). The saturation magnetization M_{sat} of $1.2 \times 10^6 \text{ J m}^{-3} \text{ T}^{-1}$ agrees with the bulk value reported in the literature^{21,23}. The t dependence of M_{sat} at temperature $T = 400$ K (Fig. 1g) shows that the M_{sat} decreases below $t = 0.80$ nm. However, the bulk-like M_{sat} value at low T (see Supplementary Fig. 5 for the T dependence of M_{sat}) persists down to $t = 0.32$ nm, indicating that Fe spins order ferromagnetically even in these ultrathin samples. The M_{sat} significantly decreases at $t = 0.24$ nm. The clear qualitative change in the magnetic behavior occurs between $t = 0.32$ nm and 0.24 nm. Combined with the TEM results (Fig. 1d and Supplementary Fig. 3), this implies that the nominal t value corresponds to the actual film thickness even in these ultrathin films. The estimated T_c is significantly higher than 400 K for $t \geq 0.48$ nm and becomes comparable to 400 K for $0.32 \text{ nm} \leq t \leq 0.40$ nm. A more detailed analysis of the T dependence of magnetization across the ferromagnetic transition will clarify the accurate T_c and possible role of disorder on the magnetic behavior²⁴.

Thickness-dependent magnetic anisotropy in $\text{Fe}_3\text{Sn}/\text{Pt}$ bilayers.

By comparing M versus $\mu_0 H$ curves in out-of-plane and in-plane configurations, we detected the expected variation of magnetic anisotropy, as displayed in Fig. 2a–c. For $t = 0.64$ nm (Fig. 2a), the M saturates easily under the application of in-plane H (blue curve), showing the in-plane magnetic anisotropy consistent with the bulk behavior²¹. In the sample with $t = 0.48$ nm (Fig. 2b), however, the M saturates at almost comparable $\mu_0 H$ values in the two measurement configurations. The even thinner condition of $t = 0.24$ nm appears to favor perpendicular magnetic anisotropy (Fig. 2c). From the M/M_{sat} versus $\mu_0 H$ curves, we calculated the magnetic anisotropy energy as the effective anisotropy field $\mu_0 H_{A,\text{eff}}$ in the unit of T ($\mu_0 H_{A,\text{eff}} > 0$ for perpendicular magnetic anisotropy and < 0 for in-plane magnetic anisotropy). As plotted in Fig. 2d, $\mu_0 H_{A,\text{eff}}$ gradually varies from negative to positive with decreasing t , changing its sign at approximately 0.5 nm (~ 1 unit cell). This result captures that the inherent in-plane magnetic anisotropy turns to perpendicular magnetic anisotropy at a crossover thickness of $t_{\text{MA}} \sim 0.5$ nm. To gain insight into spin textures in these ultrathin Fe_3Sn bilayer samples, we performed a numerical simulation for a single kagome plane that took into account the ferromagnetic Heisenberg interaction J , magnetic anisotropy A (in-plane and perpendicular magnetic anisotropy for $A < 0$ and > 0 , respectively), and DMI (see Methods). As schematically shown in Fig. 2e, this model considers spin interactions between the neighboring spins on the kagome plane in an out-of-plane magnetic field. Bulk and interfacial DMIs contribute to the out-of-plane and in-plane components of \mathbf{D} (D_{\parallel} and D_{\perp}), respectively, which modifies the local spin interactions to produce a finite spin solid angle. Figure 2f displays the total spin solid angle per the unit cell of Fe_3Sn , $|\Omega_{\text{tot}}|$, as a function of A and D_{\perp} ($J = D_{\parallel} = 1$ and out-of-plane magnetic field $g\mu_B H = 0.05$, where g is the g -factor and μ_B is the Bohr magneton). In the upper-left region of large negative A and small D_{\perp} , the spins basically lie in the kagome plane

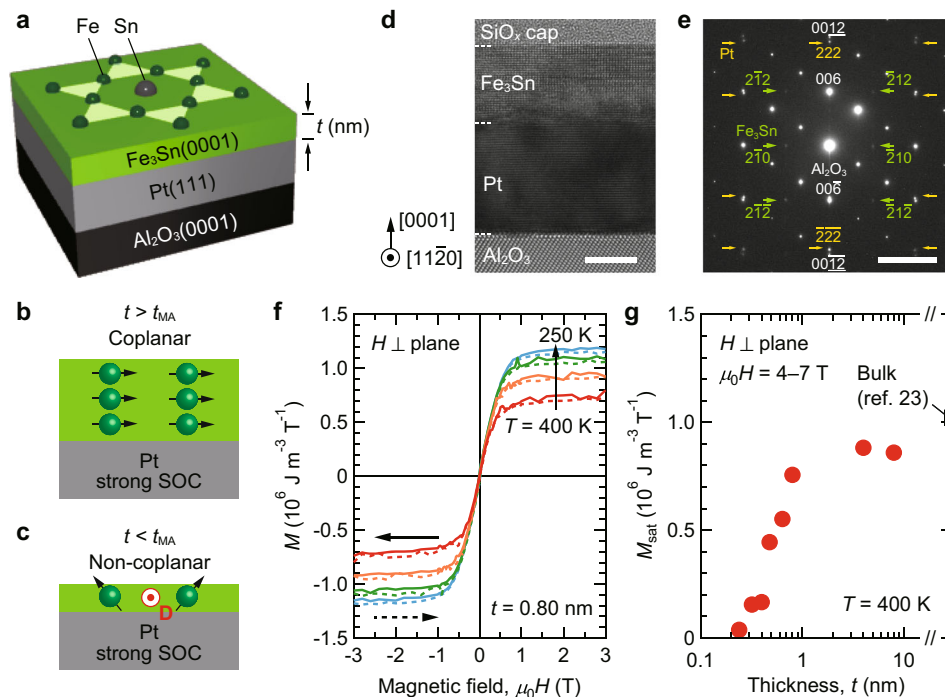


Fig. 1 Kagome-lattice ferromagnet $\text{Fe}_3\text{Sn}/\text{Pt}$ bilayer. **a** Schematic structure of $\text{Fe}_3\text{Sn}(t \text{ nm})/\text{Pt}(10 \text{ nm})$ bilayer on $\text{Al}_2\text{O}_3(0001)$. A SiO_x cap layer is not drawn for simplicity. **b, c** Concept of the scalar spin chirality driven by the interfacial DMI. Above t_{MA} , bulk-like in-plane magnetic anisotropy stabilizes a coplanar spin state with no scalar spin chirality. Below t_{MA} , the interfacial DMI modifies the magnetic anisotropy, inducing a non-coplanar spin state with finite scalar spin chirality. **d** Cross-sectional TEM image of a bilayer sample with $t = 8 \text{ nm}$ viewed along $\text{Al}_2\text{O}_3[11\bar{2}0]$. Scale bar, 5 nm. **e** Selected-area electron diffraction pattern including the film and substrate regions. Scale bar, 5 nm $^{-1}$. **f** M versus μ_0H curves for $t = 0.80 \text{ nm}$ measured at $T = 400, 350, 300,$ and 250 K in an out-of-plane H configuration. The solid and dashed curves correspond to the decreasing-field and increasing-field scans, as shown by the black solid and dashed arrows, respectively. **g** t dependence of M_{sat} at $T = 400 \text{ K}$ in an out-of-plane H configuration. The M_{sat} is averaged over $\mu_0H = 4\text{--}7 \text{ T}$. The bulk M_{sat} is calculated from the mass magnetization data in ref. 23 using the reported density of 8.45 g cm^{-3} (JCPDS PDF 01-074-5857).

with slightly tilting to the out-of-plane H direction (see Supplementary Fig. 6 for the simulated magnetic moments). This corresponds to a ferromagnetically ordered phase with in-plane magnetic anisotropy in the kagome plane as in the bulk²¹. Increasing A to the positive side stabilizes a different ordered phase where spins fully point to the out-of-plane H direction. Although these ordered phases do not generate $|\Omega_{\text{tot}}|$, we found that a moderate contribution of D_{\perp} stabilizes a two-dimensional SkX phase with a finite $|\Omega_{\text{tot}}|$ (inset, also see Supplementary Fig. 7). By a further increase of D_{\perp} , the spiral phase without a finite $|\Omega_{\text{tot}}|$ is induced. This magnetic phase diagram highlights the critical importance of the interface-driven modification of DMI for the stabilization of SkX phase in the ferromagnetic kagome lattice. In fact, the clear switching of magnetic anisotropy shown in Fig. 2d corroborates that our t -controlled $\text{Fe}_3\text{Sn}/\text{Pt}$ bilayers are an excellent arena for experimentally verifying scalar spin chirality via the THE analysis.

Verification of interfacial DMI. We characterized three sample structures schematically shown in Fig. 3a–c: 0.80-nm-thick $\text{Fe}_3\text{Sn}/\text{Pt}$ (thick-bilayer, $t > t_{\text{MA}}$), 0.40-nm-thick $\text{Fe}_3\text{Sn}/\text{Pt}$ (thin-bilayer, $t < t_{\text{MA}}$) and Pt/0.40-nm-thick $\text{Fe}_3\text{Sn}/\text{Pt}$ (thin-trilayer, $t < t_{\text{MA}}$; see Supplementary Fig. 8 for the M data). In the thick-bilayer and thin-bilayer structures, the interfacial DMI is activated by the bottom Pt layer, whereas in the thin-trilayer structure, the effective interfacial DMI would be canceled by opposite contributions from the top Pt/ Fe_3Sn and bottom $\text{Fe}_3\text{Sn}/\text{Pt}$ interfaces. Although there is no direct correspondence between the actual samples and simulation conditions, the thick-bilayer, thin-bilayer, and thin-trilayer structures can be compared with the simulation conditions of negative A and small D_{\perp} , small positive A and large

D_{\perp} , and small positive A and small D_{\perp} , respectively. Note here that a large part of conduction in these heterostructures is governed by the highly conducting Pt layer (See Supplementary Figs. 9 and 10 for the t -dependence of sheet resistance and the magnetoresistance data, respectively). Figure 3d shows Hall resistance R_{yx} versus μ_0H curves of the thick-bilayer structure at $T = 400 \text{ K}$. In addition to the linear ordinary Hall effect of Pt (Supplementary Fig. 11k), a nonlinear response in the R_{yx} is clearly discernable. A fit using an empirical relation^{15–19}, $R_{yx} = R_0'\mu_0H + R_A'M + R_{yx}^T$, where R_0' and R_A' are the ordinary and anomalous Hall coefficients in the unit of $\Omega \text{ T}^{-1}$, and $R_A'M (= R_{yx}^A)$ and R_{yx}^T are the anomalous and topological Hall resistances, reveals the dominant contribution of R_{yx}^A to the R_{yx} (Fig. 3e inset), which is attributed to the anomalous Hall effect (AHE) of Fe_3Sn . The negligibly small residual R_{yx}^T (Fig. 3e) indicates the absence of THE in the thick-bilayer structure. This is consistent with that the bulk-like in-plane magnetic anisotropy favors the coplanar spin state without scalar spin chirality (Fig. 1b). Contrastingly, in the thin-bilayer structure, the extracted R_{yx}^T (Fig. 3g) at $T = 400 \text{ K} \sim T_c$ (Supplementary Fig. 5) overwhelms both ordinary and anomalous Hall resistances (Fig. 3f and the inset of Fig. 3g), indicating the presence of finite scalar spin chirality that contributes to THE. The addition of top Pt layer in the thin-trilayer structure, as intended, completely diminishes the THE (Fig. 3h, i). On the other hand, the comparable AHE for the thin-trilayer and thin-bilayer structures at $T = 300 \text{ K}$ (the insets of Fig. 3f, h; also see Supplementary Fig. 11 for the data at various T) indicates their macroscopically similar ferromagnetic states. In recent studies on SrRuO_3 ultrathin films

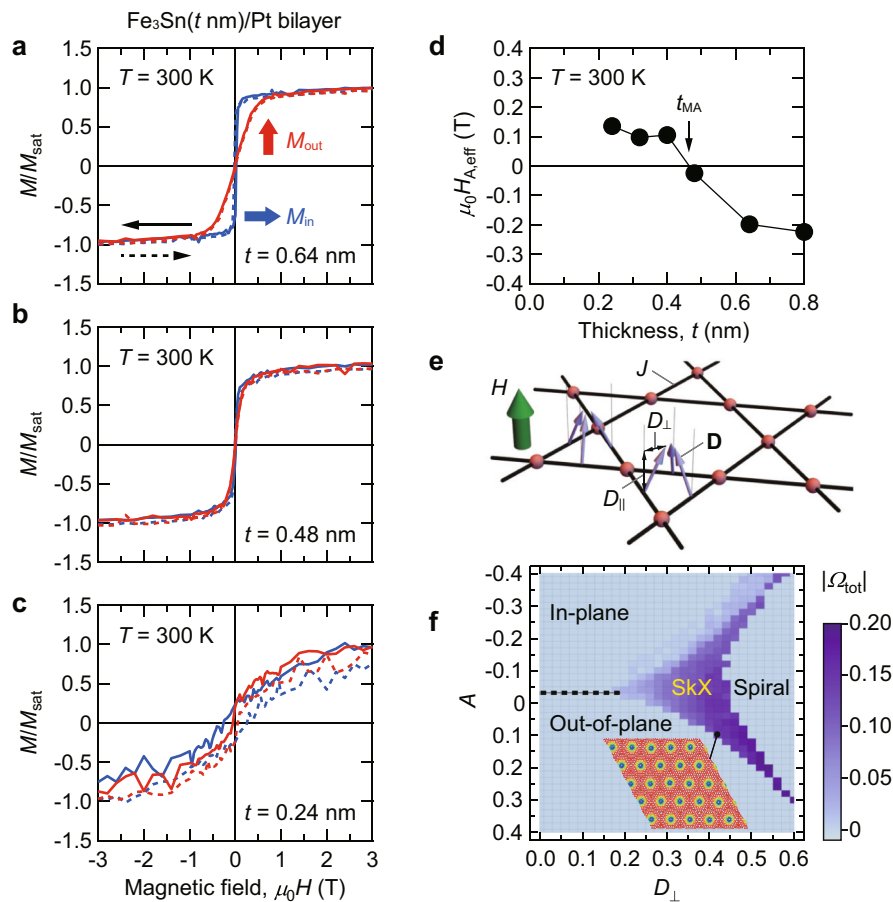


Fig. 2 Magnetic anisotropy in Fe₃Sn/Pt bilayers and magnetic phase diagram simulation. **a–c** Normalized magnetization M/M_{sat} versus $\mu_0 H$ curves measured in out-of-plane and in-plane H configurations (M_{out} and M_{in}) at $T = 300$ K for $t = 0.64$, 0.48 , and 0.24 nm, respectively. The solid and dashed curves correspond to the decreasing-field and increasing-field scans, as shown by the black solid and dashed arrows, respectively. **d** t dependence of the effective anisotropy field $\mu_0 H_{\text{A,eff}}$ calculated from the M/M_{sat} versus $\mu_0 H$ curves. **e** Schematic model of single Fe₃Sn plane used for the Monte Carlo simulation that takes into account the ferromagnetic Heisenberg interaction J , single-ion anisotropy, and in-plane and out-of-plane components of \mathbf{D} (D_{\parallel} and D_{\perp}). Pink spheres indicate Fe atoms. An external H (green arrow) is applied perpendicular to the kagome plane. **f** Simulated magnetic phase diagram of single Fe₃Sn plane. A contour plot of the spin solid angle $|\Omega_{\text{tot}}|$ integrated over the unit cell is overlaid. The used parameters are $J = D_{\parallel} = 1.0$ and $g\mu_B H = 0.05$. A dotted line indicates the boundary between the in-plane and out-of-plane phases. In-plane: a phase where spins lying in the kagome plane tilt to the applied H direction. Out-of-plane: a phase where spins fully point to the applied H direction, with no net magnetization in the kagome plane. The corresponding magnetization components are shown in Supplementary Fig. 6. Inset: typical spin texture in the SkX obtained with $A = 0.10$ and $D_{\perp} = 0.42$. The result for the spiral phase at higher D is shown in Supplementary Fig. 7.

and SrRuO₃-based perovskite multilayers and superlattices^{24–28}, the impact of inhomogeneity on the occurrence of THE-like R_{yx} anomalies has been argued. When AHE changes its sign depending on thickness as in the present system (Supplementary Fig. 11), local thickness fluctuation could give rise to hump-like R_{yx} behavior via the superposition of AHE components with different signs. To understand the origin of the observed R_{yx}^T , we evaluated asymmetric Ta/Fe₃Sn/Pt and W/Fe₃Sn/Pt trilayer structures (Supplementary Fig. 12 and Supplementary Note 1). The results were consistently explained by considering different magnitudes of the interfacial DMI contributions from the top and bottom interfaces. In conjunction with the insignificant thickness fluctuation suggested by the TEM and magnetization measurements, this strongly supports that the interfacial DMI plays a more decisive role in the occurrence of R_{yx}^T than inhomogeneity. Furthermore, the superposition of R_{yx} versus $\mu_0 H$ curves for different t values at $T = 400$ K (Supplementary Fig. 11) cannot reproduce the sharp R_{yx} peaks detected in the thin-bilayer structure (Fig. 4f). These observations are fully consistent with the generation of finite scalar spin chirality owing to the local modification of spin interactions by the interfacial DMI.

Analysis of THE and possible formation of SkX phase. Having verified the interfacial DMI origin, we demonstrate the t -controlled variation of scalar spin chirality via the detection of THE. As shown in Fig. 4a–c, a slight reduction of t effectively lowers the T range where THE appears (see Supplementary Fig. 13 for the corresponding R_{yx}^T data). Upon comparing the R_{yx} data including those of other t values (Supplementary Fig. 11), we noticed the sign reversal of R_{yx} at approximately $T = 370$ K for $t = 0.40$ nm (Fig. 4b) and at $T = 340$ K for $t = 0.32$ nm (Fig. 4c). Figure 4d shows a contour plot of $\Delta R_{yx} (\pm 3 \text{ T}) = R_{yx} (+3 \text{ T}) - R_{yx} (-3 \text{ T})$ on t - T plane; its sign reversal occurs in close proximity to the THE region (surrounded by dashed lines). According to recent band structure calculation²⁹, Fe₃Sn is classified as a magnetic Weyl semimetal with Weyl nodes³⁰ near the Fermi level. The T -induced shift of the Fermi level and the resulting change in the intrinsic AHE contribution may play a role in the T -induced sign reversal of AHE.

More importantly, as shown in Fig. 4e, the magnitude of R_{yx}^T increases with increasing T (up to our measurement limit of 400 K), concomitantly with the increase of the peak magnetic field at which R_{yx} shows local maxima/minima due to THE, $\mu_0 H_{\text{peak}}$ (black circles).

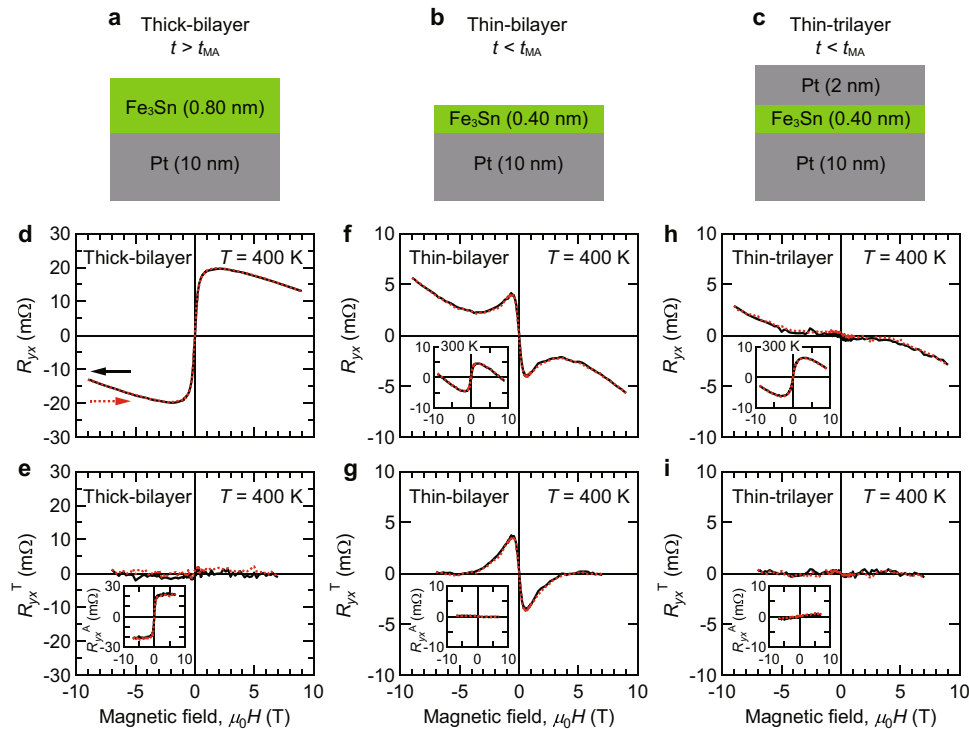


Fig. 3 Hall effect measurements. **a–c** Schematic structures of Fe_3Sn ($t = 0.80$ nm)/Pt bilayer (thick-bilayer), Fe_3Sn ($t = 0.40$ nm)/Pt bilayer (thin-bilayer), and Pt/ Fe_3Sn ($t = 0.40$ nm)/Pt trilayer (thin-trilayer), respectively. **d** R_{yx} versus μ_0H curves of the thick-bilayer structure at $T = 400$ K and **e** the extracted R_{yx}^T and R_{yx}^A (inset), **f** R_{yx} versus μ_0H curves of the thin-bilayer structure at $T = 400$ K and 300 K (inset) and **g** the extracted R_{yx}^T and R_{yx}^A (inset), **h** R_{yx} versus μ_0H curves of the thin-trilayer structure at $T = 400$ K and 300 K (inset) and **i** the extracted R_{yx}^T and R_{yx}^A (inset). The two curves corresponding to the decreasing-field and increasing-field scans are shown, which are represented by black solid and red dotted curves, respectively. Only in the thin-bilayer structure, the contribution of R_{yx}^T is observed, evidencing the interfacial DMI origin.

Using the standard linear-response theory for a Kondo-lattice model, we performed the analysis of finite-temperature Hall conductivity $|\sigma_{\text{H}}^T|$ of the intrinsic Berry phase mechanism (Fig. 4f, also see the $|\Omega_{\text{tot}}^T|$ result for Supplementary Fig. 14). Overall, the simulation results reproduce the observed experimental trend, indicating the contribution of thermal fluctuation^{18,31} to the intrinsic (topological) Hall effect. These excellent agreements between the experiments and simulation suggest the formation of SkX phase in the THE region. To support this, we attempted to extract real-space features from the THE data using the relation^{5,16,17}: $\rho_{yx}^T = PR_0 n_{\text{sk}} \phi_0$, where ρ_{yx}^T is the topological Hall resistivity, P is the spin polarization, R_0 is the ordinary Hall coefficient, n_{sk} is the skyrmion density, and ϕ_0 is one magnetic flux quantum ($= h/e$ with h being the Planck constant and e being the elementary charge). The $n_{\text{sk}}^{-0.5}$ corresponds to the average separation of skyrmions. Assuming a parallel circuit consisting of two conducting layers, we calculated the resistivity and Hall resistivity (Supplementary Fig. 15) of the Fe_3Sn layer from the 0.40-nm-thick bilayer data and reference Pt monolayer data at $T = 350$ K, yielding $\rho_{yx}^T = 37.4$ n Ω cm and $R_0 = 8.48 \times 10^{-5}$ cm³ C⁻¹. These values give $n_{\text{sk}}^{-0.5} = 9.68$ nm and 30.6 nm for $P = 0.1$ and 1, respectively, which are reasonable as compared with the size of skyrmions reported for other bilayer systems (Supplementary Table 1). We therefore think that densely arranged skyrmions like SkX exist in the $\text{Fe}_3\text{Sn}/\text{Pt}$ bilayer samples. Direct observation of the spin textures using microscopy will be an interesting future study.

Conclusion

The epitaxial interface of kagome-lattice ferromagnet Fe_3Sn and Pt enables the rational control of magnetic and electrical properties based on the interfacial DMI. Considering the rich variety of kagome-lattice magnets such as Fe_3Sn_2 , FeSn , and $\text{Co}_3\text{Sn}_2\text{S}_2$

that have been discovered from the aspect of topological physics, the development of heterointerfaces and superlattices is worthy of investigation. These fascinating features of kagome-lattice magnets will offer tremendous opportunities for exploring new functionalities of SkX-based phenomena.

Methods

Thin-film growth. The films were fabricated on $\text{Al}_2\text{O}_3(0001)$ substrates by radio-frequency magnetron sputtering at an Ar gas pressure of 0.5 Pa. The Pt, Fe_3Sn , and SiO_x layers were in situ deposited at 600, 400, and 100 °C with Pt, Fe-Sn [ref. 32], and SiO_x targets, respectively. The 2-nm-thick Pt top layer of the thin-trilayer structure (Fig. 3c) was deposited at 100 °C before the SiO_x capping. The crystal structure of the films was characterized by TEM and X-ray diffraction using Cu K_α radiation. The t values were calculated based on the sputtering rate that was calibrated with the cross-sectional TEM image shown in Fig. 1d.

Measurements. The magnetization was measured with a superconducting quantum interference device magnetometer (MPMS3, Quantum Design) upon decreasing μ_0H from 7 T to -7 T and increasing μ_0H from -7 T to 7 T. By subtracting a diamagnetic contribution from Al_2O_3 substrate, which was estimated from the high-field data at $\mu_0H = 4\text{--}7$ T, the M was calculated. By anti-symmetrizing the decreasing-field and increasing-field M data, the two anti-symmetrized M curves shown in Figs. 1f and 2a–c and Supplementary Figs. 4 and 8 were obtained. The electrical properties were measured with a physical property measurement system (PPMS, Quantum Design). The films were patterned into a Hall-bar shape by mechanical scratch, and electrical contacts were made with indium solder. For the analysis of THE, the decreasing-field and increasing-field R_{yx} data were anti-symmetrized against μ_0H to eliminate spurious contributions arising from thermoelectric effect and misalignment of the Hall voltage probes.

Simulation. We considered a classical Heisenberg model on the kagome lattice to understand the magnetism of Fe_3Sn thin films. The Hamiltonian reads

$$H = \sum_{\langle i,j \rangle} [-J\mathbf{S}_i \cdot \mathbf{S}_j - \mathbf{D}_{ij} \cdot \mathbf{S}_i \times \mathbf{S}_j] + \sum_i [-A(S_i^z)^2 - g\mu_B H S_i^z], \quad (1)$$

where \mathbf{S}_i represents a classical spin with fixed length $|\mathbf{S}_i| = 1$ on i th site. The first sum of $\langle i,j \rangle$ runs over all the nearest neighbor sites; J and \mathbf{D}_{ij} represent the ferromagnetic

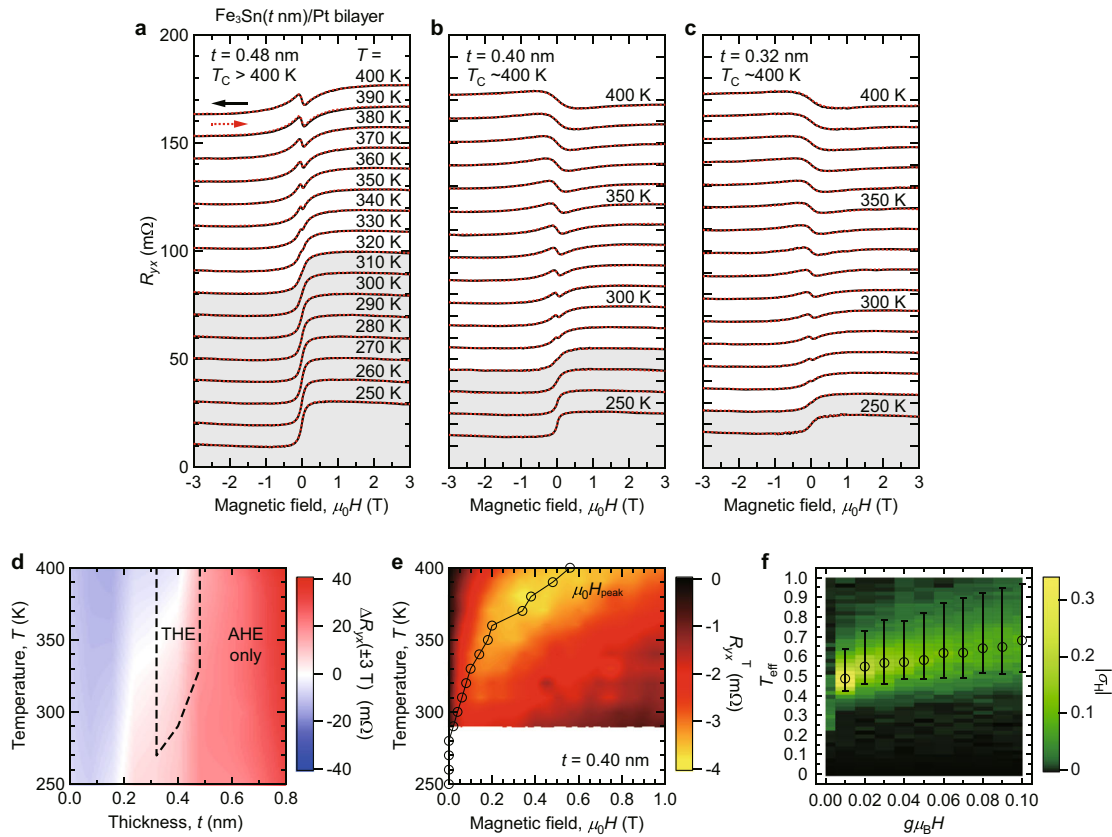


Fig. 4 Analysis of T- and t-dependent THE. **a-c** R_{yx} versus $\mu_0 H$ curves measured at $T = 400\text{--}250$ K for $t = 0.48, 0.40$ and 0.32 nm, respectively. The two curves corresponding to the decreasing-field and increasing-field scans are shown, which are represented by black solid and red dotted curves, respectively. The data are shifted vertically for clarity. The gray-shaded regions represent the T range where no clear THE signals are discerned. **d** Contour plot of $\Delta R_{yx} (\pm 3 T)$ as a function of t and T , which is produced from all data for $t = 0.80\text{--}0$ nm. The THE region indicated by the dashed lines corresponds to the unshaded data in Fig. 4a-c. **e** Contour plot of R_{yx}^T as a function of $\mu_0 H$ and T for $t = 0.40$ nm. The $\mu_0 H_{\text{peak}}$ values at which $|R_{yx}^T|$ becomes maximal are shown by black circles. **f** Finite-temperature Hall conductivity σ_H calculated using the Monte Carlo simulation and the linear-response theory with a Kondo lattice model. The used parameters are $J = D_{\parallel} = 1.0, A = 0.1$, and $D_{\perp} = 0.25$. Here, T_{eff} is the effective temperature against J . The electron temperature and the electron filling number (up to 2 per site) are set to 0.025 and 0.1, respectively. Black spheres represent the temperature at which $|\sigma_H|$ becomes maximal, and error bars correspond to the full width at half maximum.

Heisenberg coupling and the DMI, respectively. The second sum represents the single ion anisotropy A and the Zeeman coupling to the external magnetic field H perpendicular to the kagome plane. We set the direction of \mathbf{D}_{ij} as shown in Fig. 2e from the symmetry point of view⁸. The out-of-plane component D_{\parallel} is inherent to the inversion symmetry breaking on the bond centers on the kagome lattice (bulk DMI), while in-plane component D_{\perp} arises from the breaking of mirror symmetry due to the attached Pt layer (interfacial DMI). Note that the latter satisfies C_3 and C_6 rotational symmetries around the center of the triangular and hexagonal plaquettes of the kagome lattice, respectively. We adopted $J = D_{\parallel}$; similar conditions have been used in previous studies^{33,34}. The magnetic field H was set to be weak so that the magnetization is not forced to be parallel to the applied H direction. In the finite-temperature analysis shown in Fig. 4f, we set $D_{\perp} = 0.25 < J = D_{\parallel}$. Because D_{\perp} is a contribution that is effective only at the interface, this assumption is qualitatively valid. Positive and negative D_{\perp} gave the identical simulation results. As for the single-ion anisotropy A , we set $A = 0.1$ by considering the saturation field ~ 0.5 T and $T_C \geq 400$ K (i.e., $A \ll J$) in the experimental magnetization data.

To obtain the ground-state spin configuration of (1), we used a combined method of simulated annealing and local optimization. The annealing was performed from the temperature 1 to 0.001 with 100 steps in the logarithmic scale. In each step, we spent 1000 Monte Carlo (MC) sweeps. After the annealing, we optimized the spin directions one by one so as to minimize the local energy with fixed surrounding spins. We repeated 20000 sweeps of this optimization process. For analyzing the finite-temperature properties, we performed MC simulations with 100000 MC sweeps after 100000 thermalization at each temperature. In all the calculations, we considered $N = 3L^2$ spins with $L = 48$ under the periodic boundary condition.

To detect the non-coplanar spin structure in the SkX, we computed the solid angle defined as

$$\Omega_{\text{tot}} = \frac{1}{L^2} \left[\sum_{(i,j,k)} \Omega_{ijk} + \sum_{(i,j,k,l,m,n)} (\Omega_{ijk} + \Omega_{ikl} + \Omega_{ilm} + \Omega_{imn}) \right] \quad (2)$$

with the solid angle³⁵

$$\Omega_{ijk} = 2 \arctan \left(\frac{\mathbf{S}_i \cdot \mathbf{S}_j \times \mathbf{S}_k}{1 + \mathbf{S}_i \cdot \mathbf{S}_j + \mathbf{S}_j \cdot \mathbf{S}_k + \mathbf{S}_k \cdot \mathbf{S}_i} \right), \quad (3)$$

which is defined in the range of $(-2\pi, 2\pi)$. The sums of (i, j, k) and (i, j, k, l, m, n) run over all the triangular and hexagonal plaquettes of the kagome lattice, respectively, in which i, j, \dots were assigned in the counterclockwise order when viewed from the z direction. We also computed the magnetizations (Supplementary Fig. 6):

$$m_z = \frac{1}{N} \sum_i \langle S_i^z \rangle, \quad m_{xy} = \frac{1}{N} \sqrt{\left\langle \left(\sum_i S_i^x \right)^2 \right\rangle + \left\langle \left(\sum_i S_i^y \right)^2 \right\rangle}. \quad (4)$$

We calculated the Hall conductivity σ_H for the spin configurations obtained by the MC simulations. For this purpose, we introduced the Kondo lattice model;

$$\mathcal{H}_{\text{KLM}} = -t_K \sum_{\langle i,j \rangle, s} [c_{is}^\dagger c_{js} + \text{h.c.}] - J_H \sum_{i,s,s'} (c_{is}^\dagger \sigma_{ss'} c_{is'}) \cdot \mathbf{S}_i \quad (5)$$

with the given spin configurations \mathbf{S}_i , and computed σ_H by using the standard Kubo formula. The first term represents the kinetic energy of itinerant electrons with the nearest neighbor hopping t_K , and the second term represents the Hund's coupling J_H between itinerant electron spins defined by the Pauli matrices σ and localized spins \mathbf{S}_i . In the calculations, we took $J_H = 4t_K$ and fixed the electron density at $n_{\text{el}} = \sum_{i,s} \langle c_{is}^\dagger c_{is} \rangle / N = 0.1$. This low n_{el} is regarded as a dilute limit^{36,37}, which is appropriate to capture the generic feature of the single kagome plane. For simplicity, we set the temperature of the itinerant electrons sufficiently low as $T_{\text{KLM}} = t_K/40$ to focus on the fluctuations of spins.

Data availability

The data that support the findings of this study are available from the corresponding author upon reasonable request.

Received: 15 April 2021; Accepted: 19 October 2021;

Published online: 09 November 2021

References

- Loss, D. & Goldbart, P. M. Persistent currents from Berry's phase in mesoscopic systems. *Phys. Rev. B* **45**, 13544–13561 (1992).
- Ye, J. et al. Berry phase theory of the anomalous Hall effect: application to colossal magnetoresistance manganites. *Phys. Rev. Lett.* **83**, 3737–3740 (1999).
- Taguchi, Y., Oohara, Y., Yoshizawa, H., Nagaosa, N. & Tokura, Y. Spin chirality, Berry phase, and an anomalous Hall effect in a frustrated ferromagnet. *Science* **291**, 2573–2576 (2001).
- Nagaosa, N. & Tokura, Y. Topological properties and dynamics of magnetic skyrmions. *Nat. Nanotechnol.* **8**, 899–911 (2013).
- Kanazawa, N., Seki, S. & Tokura, Y. Noncentrosymmetric magnets hosting magnetic skyrmions. *Adv. Mater.* **29**, 1603227 (2017).
- Bogdanov, A. N. & Panagopoulos, C. Physical foundations and basic properties of magnetic skyrmions. *Nat. Rev. Phys.* **2**, 492–498 (2020).
- Dzialoshinskii, I. E. Thermodynamic theory of 'Weak' ferromagnetism in antiferromagnetic substances. *J. Exp. Theor. Phys.* **5**, 1547–1562 (1957).
- Moriya, T. Anisotropic superexchange interaction and weak ferromagnetism. *Phys. Rev.* **120**, 91–98 (1960).
- Soumyanarayanan, A., Reyren, N., Fert, A. & Panagopoulos, C. Emergent phenomena induced by spin-orbit coupling at surfaces and interfaces. *Nature* **539**, 509–517 (2016).
- Fert, A., Reyren, N. & Cros, V. Magnetic skyrmions: advances in physics and potential applications. *Nat. Rev. Mater.* **2**, 17031 (2017).
- Jiang, W. et al. Blowing magnetic skyrmion bubbles. *Science* **349**, 283–286 (2015).
- Moreau-Luchaire, C. et al. Additive interfacial chiral interaction in multilayers for stabilization of small individual skyrmions at room temperature. *Nat. Nanotechnol.* **11**, 444–448 (2016).
- Boulle, O. et al. Room-temperature chiral magnetic skyrmions in ultrathin magnetic nanostructures. *Nat. Nanotechnol.* **11**, 449–454 (2016).
- Woo, S. et al. Observation of room-temperature magnetic skyrmions and their current-driven dynamics in ultrathin metallic ferromagnets. *Nat. Mater.* **15**, 501–506 (2016).
- Soumyanarayanan, A. et al. Tunable room-temperature magnetic skyrmions in Ir/Fe/Co/Pt multilayers. *Nat. Mater.* **16**, 898–904 (2017).
- Raju, M. et al. The evolution of skyrmions in Ir/Fe/Co/Pt multilayers and their topological Hall signature. *Nat. Commun.* **10**, 696 (2019).
- Matsuno, J. et al. Interface-driven topological Hall effect in SrRuO₃-SrIrO₃ bilayer. *Sci. Adv.* **2**, e1600304 (2016).
- Wang, W. et al. Spin chirality fluctuation in two-dimensional ferromagnets with perpendicular magnetic anisotropy. *Nat. Mater.* **18**, 1054–1059 (2019).
- Yasuda, K. et al. Geometric Hall effects in topological insulator heterostructures. *Nat. Phys.* **12**, 555–559 (2016).
- Heinze, S. et al. Spontaneous atomic-scale magnetic skyrmion lattice in two dimensions. *Nat. Phys.* **7**, 713–718 (2011).
- Sales, B. C., Saporov, B., McGuire, M. A., Singh, D. J. & Parker, D. S. Ferromagnetism of Fe₃Sn and alloys. *Sci. Rep.* **4**, 7024 (2014).
- Maeno, A. et al. Fabrication of X₃Sn (X = Fe, Mn) epitaxial films and the magnetic and electronic properties. *Extended Abstracts of the 80th Autumn Meeting, The Japan Society of Applied Physics* 18p-E216-16 (2019).
- Echevarria-Bonet, C. et al. Structural and magnetic properties of hexagonal Fe₃Sn prepared by non-equilibrium techniques. *J. Alloys Compd.* **769**, 843–847 (2018).
- Yang, L. et al. Origin of the hump anomalies in the Hall resistance loops of ultrathin SrRuO₃/SrIrO₃ multilayers. *Phys. Rev. Mater.* **5**, 014403 (2021).
- Wang, L. et al. Controllable thickness inhomogeneity and Berry curvature engineering of anomalous Hall effect in SrRuO₃ ultrathin films. *Nano Lett.* **20**, 2468–2477 (2020).
- Wu, P. C. et al. Thickness dependence of transport behaviors in SrRuO₃/SrTiO₃ superlattices. *Phys. Rev. Mater.* **4**, 014401 (2020).
- Groenendijk, D. J. et al. Berry phase engineering at oxide interfaces. *Phys. Rev. Res.* **2**, 023404 (2020).
- Zheng, D. et al. Berry phase engineering in SrRuO₃/SrIrO₃/SrTiO₃ superlattices induced by band structure reconstruction. *ACS Nano* **15**, 5086–5095 (2021).
- Karki, B., Belbase, B. P. & Ghimire, M. P. Novel topological Weyl semimetallic phase in layered materials: Fe₂Sn, Fe₃Sn. In *The 2nd International Online Conference on Crystals session Crystalline Materials* 7719 https://doi.org/10.3390/iocc_2020-07719 (2020).
- Yan, B. & Felser, C. Topological materials: Weyl semimetals. *Annu. Rev. Condens. Matter Phys.* **8**, 337–354 (2017).
- Kato, Y. & Ishizuka, H. Colossal enhancement of spin-chirality-related Hall effect by thermal fluctuation. *Phys. Rev. Appl.* **12**, 021001 (2019).
- Satake, Y., Fujiwara, K., Shiogai, J., Seki, T. & Tsukazaki, A. Fe-Sn nanocrystalline films for flexible magnetic sensors with high thermal stability. *Sci. Rep.* **9**, 3282 (2019).
- Buhrandt, S. & Fritz, L. Skyrmion lattice phase in three-dimensional chiral magnets from Monte Carlo simulations. *Phys. Rev. B* **88**, 195137 (2013).
- Chisnell, R. et al. Topological magnon bands in a kagome lattice ferromagnet. *Phys. Rev. Lett.* **115**, 147201 (2015).
- Van Oosterom, A. & Strackee, J. The solid angle of a plane triangle. *IEEE Trans. Biomed. Eng.* **30**, 125–126 (1983).
- Akagi, Y. & Motome, Y. Spin chirality ordering and anomalous Hall effect in the ferromagnetic Kondo lattice model on a triangular lattice. *J. Phys. Soc. Jpn.* **79**, 083711 (2010).
- Göbel, B., Mook, A., Henk, J. & Mertig, I. Unconventional topological Hall effect in skyrmion crystals caused by the topology of the lattice. *Phys. Rev. B* **95**, 094413 (2017).

Acknowledgements

The authors thank S. Ito for the TEM analysis and N. Kanazawa for helpful discussions. This work was supported by JST CREST (JPMJCR18T2), JSPS KAKENHI Grant-in-Aid for Scientific Research (S) (JP18H05246) and (B) (20H01830), SEI Group CSR Foundation, and Foundation for Interaction in Science and Technology.

Author contributions

K.F. grew the films and characterized their structural, magnetic, and electrical properties. T.S. and K.T. contributed to the magnetization measurements and analysis. Y.K. and Y.M. performed the Monte Carlo simulation and the calculation using the linear-response theory. K.N. contributed to theoretical interpretations of the experimental results. K.F., Y.K., Y.M. and A.T. wrote the manuscript with input from other authors. A.T. supervised the project.

Competing interests

The authors declare no competing interests.

Additional information

Supplementary information The online version contains supplementary material available at <https://doi.org/10.1038/s43246-021-00218-y>.

Correspondence and requests for materials should be addressed to Kohei Fujiwara.

Peer review information *Communications Materials* thanks Wenbo Wang, M Raju and Chunruo Duan for their contribution to the peer review of this work. Primary Handling Editors: Aldo Isidori. Peer reviewer reports are available.

Reprints and permission information is available at <http://www.nature.com/reprints>

Publisher's note Springer Nature remains neutral with regard to jurisdictional claims in published maps and institutional affiliations.

 **Open Access** This article is licensed under a Creative Commons Attribution 4.0 International License, which permits use, sharing, adaptation, distribution and reproduction in any medium or format, as long as you give appropriate credit to the original author(s) and the source, provide a link to the Creative Commons license, and indicate if changes were made. The images or other third party material in this article are included in the article's Creative Commons license, unless indicated otherwise in a credit line to the material. If material is not included in the article's Creative Commons license and your intended use is not permitted by statutory regulation or exceeds the permitted use, you will need to obtain permission directly from the copyright holder. To view a copy of this license, visit <http://creativecommons.org/licenses/by/4.0/>.

© The Author(s) 2021